Fe^{3+} doped ZnO nanostructures for improved photocatalytic degradation of malachite green, crystal violet and antibacterial activity

Abhijeet R. Pawar[1], Kahkashan R. Shaikh[1], Akash D. Salmote[1], and Prabhakar B. Undre[1,*]

[1] *Department of Physics, Dr. Babasaheb Ambedkar Marathwada University, Aurangabad 431004, India*

ABSTRACT

In this work, a series of highly efficient Fe^{3+} doped ZnO nanoparticles (NPs) were synthesized using Coprecipation. The structure and morphology of the NPs were characterized by various methods, including X-ray diffraction, Field Emission Scanning Electron Microscopy (FESEM), Fourier Transform Infrared Spectroscopy, BET analysis and UV–Vis Spectroscopy. FESEM reveals a strong correlation between Fe concentration and the morphology of NPs. Nano flowerlike structure of ZnO changed to spherical NPs with Fe doping which is also evident from the observed enhancement of surface area in BET analysis. Fe^{3+} ions also caused the lowering of the optical band gap of ZnO NPs. The photocatalytic testing of the nanocatalysts is carried out using a high-intensity UV lamp (450 W) with cationic dyes [namely Malachite Green (MG) and Crystal Violet (CV)]. Among the prepared samples, 5% Fe-doped ZnO exhibited the highest photocatalytic degradation efficiency against MG dye (99.05% degradation in 20 min) and CV dye (96.85% degradation in 20 min). The antibacterial test demonstrated similar results with a dramatically improved bactericidal effect of 5% Fe: ZnO NPs over pristine ZnO NPs.

1 Introduction

In recent decades, the rapid development of industries has caused a large amount of generation of wastewater. This has led to severe worries for human life about water contamination. Dyes, one of the major categories of water pollutants, are widely employed in the production of textiles, ink and dyes for printing. Because they take a long time to break down biologically and chemically, dyes can be harmful to human health even at low concentrations [1, 2]. Malachite green (Fig. 1a) (listed in Pub CHEM as CID 11295) [3] and Crystal

Violet (Fig. 1b) (listed in Pub CHEM as CID 23424024) [4] are widely used in textiles and paper industries and are highly toxic, carcinogenic, mutagenic etc. [5, 6]. Traditional methods for treating wastewater include filtering, flocculation, sedimentation etc. [7], and with increasing amounts of waste, these methods are not sufficient anymore.

So, recently semiconductor photocatalysis has been an area of huge interest. This method has shown promising results in the fields of photocatalysis [8, 9], optoelectronics [10, 11], gas sensing etc. [12, 13]. Compared to commercial TiO$_2$ though, ZnO shows low

Springer

Fig. 1 Chemical structures of **a** Malachite Green, **b** Crystal Violet
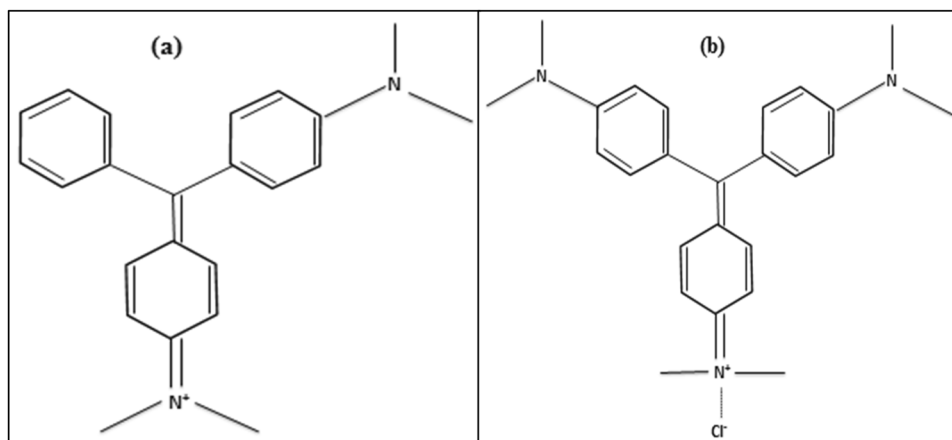
photoactivity. So, improving the activity and stability of ZnO nanoparticles is essential. Many methods have been reported in the literature for improving the photocatalytic activity of metal oxide nanocatalysts such as metal doping [14–16], non-metal doping [17, 18], making composites with other semiconductors [19, 20], polymer composite formation [21, 22], use of support systems [23, 24] or some combination of above methods [25]. In recent times, properties of ZnO nanoparticles doped with transition metals such as Ti [26, 27], Cr [28], Mn [29], Ag [30], Co and Ni [31] etc. have been studied. Various researchers have also shown improved photocatalytic activity of the ZnO nanoparticles after Iron doping. Reddy et al. synthesized Fe doped ZnO using ball milling technique which required 5 h to degrade 98.7% of the Methyl Orange dye under solar irradiation [32]. Liu et al. [33] synthesized ZnO nanofibers using electro-spinning method with dopant concentrations 0.5, 1, 1.5, 2%. Best among these was 1.5% which needed 5 h for 90% degradation of Methylene Blue. Along with these, metal oxide nanoparticles are synthesized via hydrothermal [34], solvothermal [35], sol–gel [36], gas phase methods [37] etc. Even if these studies showed improvement in the photocatalytic activity of ZnO after Fe doping, there are issues present in the synthesis methods such as long reaction time, higher temperature and energy requirements or higher costs. The Coprecipitation method is also one of the widely used methods that can be carried out at low temperatures and at low costs [38]. It also is advantageous over other techniques for doping as the reagents are mixed at the molecular level, thus providing better control over stoichiometry, homogeneity and morphology [39]. Mittal et al. used coprecipitation for doping Cu ions into the ZnO

crystals for the degradation of Crystal Violet under UV and visible light sources and found an increase in the photocatalytic activity to achieve the maximum degradation of 96.5% in 3.5 h [40]. Anju Chanu et al. managed to degrade 99% of the Methylene Blue dye in 120 min [29]. Roguai S. et al. used a simple Coprecipitation method for synthesizing Fe doped ZnO and in fact, observed a decrease in photocatalytic activity [41] compared to pristine ZnO.

This work attempts to utilize the Fe^{3+} ions to introduce defects in the ZnO crystals for the degradation of Malachite Green and Crystal Violet. Quantitative analysis of the rate kinetics of these dyes under UV irradiation is carried out. Using the Coprecipitation method at room temperature, synthesis of Fe-doped ZnO photocatalysts with varying percentages of Fe (0%, 1%, 2.5%, 5%, 7.5%) has been carried out. Further, investigations have been carried out to study the influences of Fe doping on the structural parameters, morphology and photocatalytic performance. Remarkable shifts in the photocatalytic degradation rate constant were seen after doping. Correlations of these shifts with crystalline size, morphology, specific surface area and optical properties have been studied.

2 Materials and methods

2.1 Materials

Aqueous Coprecipitation method was used for synthesis of pristine ZnO as well as Fe doped ZnO nanoparticles. Zinc Nitrate Hexahydrate $Zn(NO_3)_2 \cdot 6H_2O$ (AR Grade, Purity > 99.00%), Ferrous Nitrate Heptahydrate $FeNO_3 \cdot 7H_2O$ (AR Grade, Purity > 99.00%), Malachite

Green (AR Grade), Crystal Violet (AR Grade) and Sodium Hydroxide NaOH (LR Grade) were purchased as starting materials and used without further purification.

2.2 Preparation of Fe/ZnO nanoparticles

For the preparation of pristine ZnO nanoparticles, $Zn(NO_3)_2 \cdot 6H_2O$ was added into 100 ml of deionized water to form 0.1 M of solution and stirred for 30 min to form the precursor solution. 1 M NaOH was prepared separately in 125 ml deionized water and was added drop wise into the precursor solution at the rate of 5 ml/min under vigorous stirring to form a white precipitate. The precipitate was washed several times with deionized water and ethanol to remove impurities followed by drying on a hot plate to obtain ZnO NPs. For improving crystalline ordering, the remaining powder was annealed in a muffle furnace at 400 °C for 2 h. Annealing ZnO at temperatures in the range of 400–500 °C is often used to improve the crystallinity of the material and stabilize the wurtzite phase, which is the most common phase for ZnO. This temperature range is suitable for reducing defects and promoting well-defined crystalline structures. If annealing is performed at higher temperatures (above 700 °C), the hexagonal grains disappear significantly [42].

For the synthesis of Fe doped ZnO nanocomposites, 0.1 M $Zn(NO_3)_2 \cdot 6H_2O$ and predetermined amount ($X = 0.001$ M, 0.0025 M, 0.005 M and 0.0075 M) of $FeSO_4 \cdot 7H_2O$ were dissolved in 100 ml of deionized water to form the precursor solution. Remaining procedure was followed similar to that of synthesis of pristine ZnO nanoparticles.

2.3 Characterization

The structural parameters of the synthesized nanoparticles were characterized using Bruker's D2 PHASER Diffractometer with Cu target plate with X-ray wavelength 1.5404 Å in the scan range 20–70°. Surface Morphology was further analysed by Field Emission Scanning Electron Microscopy (FESEM) using Carl Zeiss Supra 55. Elemental analysis was carried out using EDS. The Fourier Transform Infrared Spectrometer (FTIR) spectrum in the range 400–4000 cm^{-1} was evaluated by Bruker's Alpha II spectrometer. The absorbance property was evaluated using UV–Vis spectrophotometer in the range 196–1100 nm. The pore size, volume and the specific surface areas of the synthesized samples was studied by Nitrogen Absorption based on Brunauer–Emmett–Teller (BET) technique.

2.4 Photocatalytic studies

Photocatalytic activities of ZnO nanoparticles were evaluated by monitoring the degradation rate of the Malachite Green (MG) and crystal violet (CV) dye. The experiments were conducted in a 3-jacketed photoreactor vessel [35]. The innermost jacket of the reactor contained the UV radiation source (450 W, 365 nm). The middle jacket surrounding the lamp was used for circulating water in order to control the temperature of the lamp. 100 ml aqueous solutions containing the dyes MG or CV (concentration 10 PPM) and the Fe doped ZnO catalysts (concentration 200 mg/l) were placed in the outermost jacket, which was placed on a magnetic stirrer. The solutions were stirred in the dark for 30 min before turning the UV source on, to achieve adsorption–desorption equilibrium. After regular intervals (5 min), the slurry containing the dye and the nanoparticles was extracted and was centrifuged at 5000 RPM. The supernatants were analysed using UV–Vis spectrometer at the characteristic wavelengths of the MG ($\lambda_{max} = 617$ nm) and CV ($\lambda_{max} = 589$ nm) dyes.

2.5 Antibacterial studies

Antibacterial activity of pristine and doped ZnO nanoparticles were tested against gram positive bacterial strain *Staphylococcus Aureus* (NCIM 2071) and gram-negative bacterial strain *Escherichia Coli* (MTCC 1687). Disk diffusion method [43] was used for investigation of antibacterial activity. Filter discs (6 mm) loaded with 1 mg/ml concentration sample were loaded on the nutrient agar media containing petri plates and incubated at 37 °C for 24 h. Zones of inhibitions were recorded in millimetres on a Vernier Calliper after 24 h.

3 Results and discussion

3.1 Structural studies

The X-ray diffraction spectra of the samples are given in Fig. 2. Diffraction peaks corresponding to the (100), (002), (101), (102), (110), (103), (112), (201)
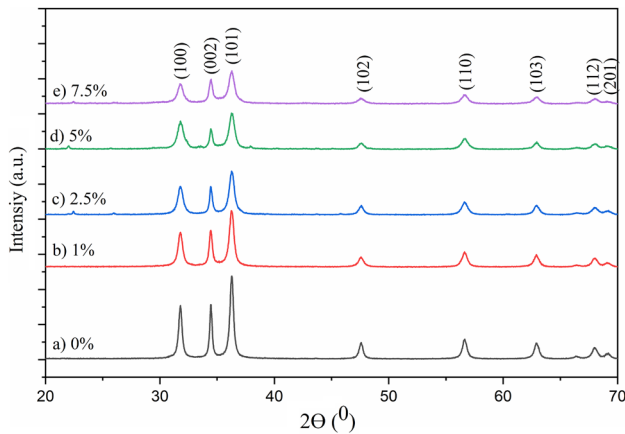
Fig. 2 XRD spectra of **a** 0%, **b** 1%, **c** 2.5%, **d** 5%, **e** 7.5% Fe doped ZnO

planes were obtained confirming the presence of hexagonal Wurtzite structure of the ZnO crystal lattice[44] (Fig. 2). The data was found to be consistent with the standard ZnO lattice with space group $P6_3mc$ (JCPDS Card No. 36-1451).

Crystalline sizes of the samples were calculated using Scherrer's formula for the sharpest peak (101). Scherrer's formula [45] for crystalline size is mentioned below:

$$\text{Crystalline Size} \, D = \frac{0.9\lambda}{\beta \cos\theta} \tag{1}$$

where λ is the wavelength of the incident radiation (k_α radiation of Cu source peaking at 1.54 Å), β is the Full Width at Half Maximum (FWHM) corresponding to the peak (here FWHM for the sharpest (101) peak has been used) and θ is the diffraction angle (2θ is the angle between incident and diffracted x-rays). Lattice parameters and the cell volume of the crystalline samples were calculated using the following formulae [46, 47] as the crystal lattice is Hexagonal Wurtzite in nature.

$$\frac{1}{d_{hkl}^2} = \left[\frac{h^2 + hk + l^2}{a^2}\right] + \frac{l^2}{c^2} \tag{2}$$

$$V = \frac{\sqrt{3}}{2}a^2c \tag{3}$$

where a, b, c are the lattice parameters (a = b for hexagonal Wurtzite structures), V is the unit cell volume, h, k, l are the Miller indices of the present peaks.
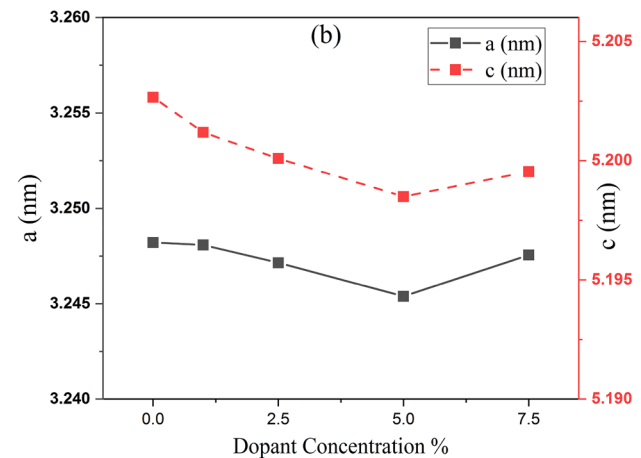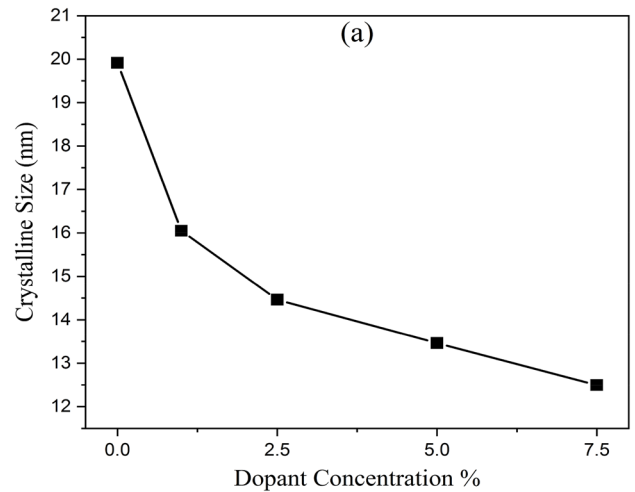

Fig. 3 Variation of **a** Crystalline Size by Scherrer's Formula, **b** lattice parameters of the ZnO samples with the dopant concentration

Presence of sharp and intense peaks confirmed presence of good crystalline nature of the nanoparticles. With increase in dopant concentration, Full Width at Half Maximum (FWHM) of the peaks increased and so, according to the Scherrer formula (Eq. 1), the crystalline size decreased (Fig. 3a). Lattice parameter a (Fig. 3b) for the pristine sample was calculated to be 3.2482 nm which decreased with the doping of the Iron and was the least for 5% doping (3.2454 nm). The lattice parameter c (Fig. 3b) also followed similar trend and was maximum for pristine ZnO (c = 5.2026 nm) and was minimum for 5% Fe doped ZnO (c = 5.1985 nm). The decrease in lattice parameters indicated the incorporation of the Fe^{2+} ions in the hexagonal ZnO lattice. Volume of the unit cell on the other hand decreased uniformly with the increase in dopant

Table 1 Variation of lattice parameters and unit cell volume with dopant concentration

Dopant concentration %	a(nm)	c(nm)	c/a	Volume of unit cell (nm³)
0	3.24820	5.20266	1.601703039	47.52479
1	3.24808	5.20118	1.601311441	47.51112
2.5	3.24714	5.20009	1.601433741	47.48388
5	3.24538	5.19849	1.60180968	47.41784
7.5	3.24755	5.19954	1.601062291	47.49076

concentration (Table 1). Table 2 shows the peak positions for different planes along with relative intensity and d-spacing. It can be observed that the centres of sharpest diffraction peaks are slightly shifted toward the higher angles.

Previous studies have shown that replacement of Zn^{2+} (0.74 Å) ions by larger Fe^{2+} (0.77 Å) ions produces significant enlargement of atomic spacing resulting in higher lattice parameters and shifting of X-ray diffraction peaks to lower angles [41, 48–50]. Contrary to this, replacement of Zn^{2+} by Fe^{3+} (0.67 Å) causes shrinking of lattice parameters and shifting of peak positions to larger angles [51–54]. Therefore, Fe: ZnO synthesized in current study shows strong presence of Fe^{3+} ions in the ZnO crystal lattice while presence of Fe^{2+} ions is weak. Also, lattice parameters and peak positions showed reversed trend while increasing dopant concentration from 5 to 7.5% indicating inefficient doping or increment in presence of Fe^{2+} ions in ZnO crystals.

3.2 FTIR studies

FTIR technique can be used to study the bond stretching and the functional groups present in the sample. Figure 4 shows the FTIR spectra of the Fe doped samples with varying fractions of Fe present. A sharp peak obtained between the 400–550 cm⁻¹ (at ~ 406 cm⁻¹) wavenumber range is attributed to Zn–O stretching [55]. Also, blue shift observed with increased Fe proportion can be caused by the replacement of certain Zn^{2+} sites with Fe^{3+} ions. Most blue shift was observed for 5% Fe doped ZnO indicating the maximum formation of Zn–O–Fe bond. All the characteristic peaks for oxides of iron [36, 56] were absent from the spectra. The cause of disappearance of peaks of dopant oxide could be explained by the presence of strong intermolecular interaction between dopant and ZnO [55].

Table 2 Variation of peak positions, peak intensities and d-spacing between the present planes

| Plane (hkl)	ZnO Position (2θ)	d spacing (Å)	Intensity (%)	1% Fe doped ZnO Position (2θ)	d spacing (Å)	Intensity (%)	2.5% Fe doped ZnO Position (2θ)	d spacing (Å)	Intensity (%)	5% Fe doped ZnO Position (2θ)	d spacing (Å)	Intensity (%)	7.5% Fe doped ZnO Position (2θ)	d spacing (Å)	Intensity (%)
100	31.78411	2.812435	64.65	31.78537	2.81292	62.20	31.79473	2.812435	65.53	31.81243	2.812435	78.74	31.79063	0.7374	62.32
002	34.45828	2.60123	65.89	34.44822	2.601331	65.66	34.46576	2.602724	65.10	34.47669	2.60123	57.66	34.46954	0.54485	75.30
101	36.2741	2.473408	100.00	36.26531	2.475049	100.00	36.27954	2.474753	100.00	36.28434	2.476105	100.00	36.25522	0.7676	100.00
102	47.57857	1.908793	20.47	47.57391	1.909768	19.21	47.58687	1.908019	22.45	47.59571	1.908019	19.47	47.5905	0.75598	21.03
110	56.6347	1.623732	24.51	56.63076	1.623951	28.20	56.64109	1.624808	30.75	56.64505	1.622657	31.64	56.63824	0.74197	30.55
103	62.92728	1.476818	19.82	62.90704	1.476179	22.98	62.92544	1.475525	22.92	62.90824	1.475525	23.00	62.90919	0.74186	23.88
112	68.01907	1.378036	14.50	68.02175	1.377098	17.30	68.22198	1.378402	18.18	68.26556	1.376944	17.44	68.0692	0.93994	19.35
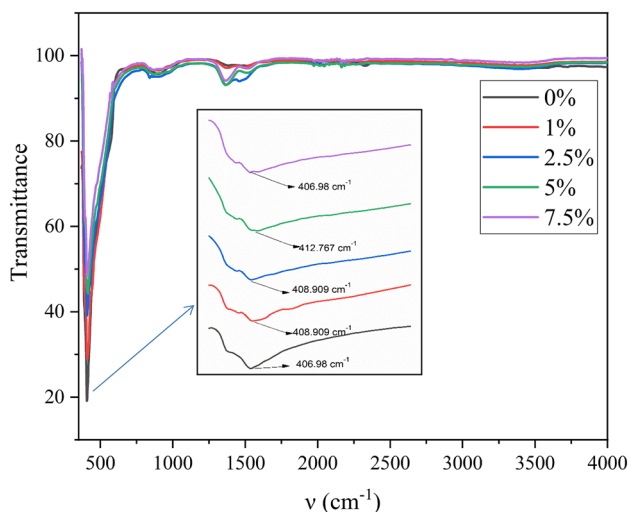
Fig. 4 FTIR spectra of the ZnO Nanopowders with varying percentages of Fe

The peak at around 1365 cm^{-1} could be ascribed to the formation of Zn–O–Fe bond as the peak is not found in pristine ZnO sample or any iron oxide sample. Absence of any other notable peak (including that of the –OH stretching of the absorbed moisture) suggests high purity of the synthesized crystalline Fe doped ZnO samples.

3.3 Morphological and elemental composition

Morphological studies of the prepared catalysts were carried out by analysing FESEM images as shown in Figs. 5 and 6. Using these images, average grain size was estimated by plotting histograms using the IMAGEJ software. The FESEM image of pristine ZnO reveals a 3D flower-like morphology with the average dimensions of 1.426 μm (Fig. 5), which is assembled from various thin 2D nanosheets. The morphology after 1% doping was a highly irregular blend of quasi-spherical and flake-like particles. However, for 2.5 and 5% Fe doped ZnO NPs, spherical shaped nanoparticles were found having average size of 20.70 and 19.65 nm respectively. Further doping to 7.5% concentration, again lead to flake like morphology with significant agglomeration with highly irregular sizes. The results all together indicate the strong influence of dopant concentration on morphology of pristine ZnO, which are in good agreement with previous reports [57–59].

Figure 7a–e represents the EDS spectra of the Fe doped ZnO nanopowders. Peaks corresponding to Fe,

Zn and O in the EDS spectra confirm the ZnO phase formation. Table 3 shows the atomic content of different elements in the nanocatalysts. Also, the stoichiometric proportions of Fe in the Fe$_x$Zn$_{1-x}$O nanostructures are represented using ratio of quantities of Fe detected to the quantities of Zn detected (Fe/Zn).

3.4 Optical properties

Figure 8a shows the UV–Vis optical absorbance spectra of Fe^{3+} doped ZnO nanoparticles. It can be seen from the absorbance spectra that the absorption in UV range increased dramatically on Fe^{3+} doping providing the foundation for higher optical activity in presence of UV region. The optical band gaps of the Fe doped ZnO nanocatalysts were further calculated using the Diffuse Reflectance UV absorbance spectra. The Tauc plot equation [60] given below was used to determine the band gap of the 0%, 1%, 2.5%, 5% and 7.5% Fe doped ZnO samples.

$$(\alpha h\nu)^2 = A(h\nu - E_g) \tag{4}$$

here, α is the absorption constant, h is the Plank's constant, ν is the frequency, E_g is the energy band gap and A is a characteristic constant of the material also known as the optical band gap. The band gaps are calculated by plotting graphs between $(\alpha h\nu)^2$ and $(h\nu)$ for all the samples. The optical band gap for undoped ZnO was found to be 3.44 eV which decreased with 1% Fe doping to 3.09 eV, 2.5% doping to 3.00 eV, 5% doping to 2.94 eV and with 7.5% doping to 2.73 eV (Fig. 8b–f). So, with increasing Fe%, a red-shift was found in the forbidden band energy of the ZnO samples. Earlier works also found the red-shift in the optical band gaps [58, 59]. This shift can mainly be attributed to exchange interactions between localized d electrons of the Fe^{2+} ions and the band electrons [58]. A negative and positive correction to conduction and valence band edges respectively could be produced due to s–d and p–d exchange interactions. This ultimately leads to the narrowing of the band gap. Also, visible light responsiveness of the ZnO catalysts improved with doping due to lowering of the band gaps.

3.5 BET studies

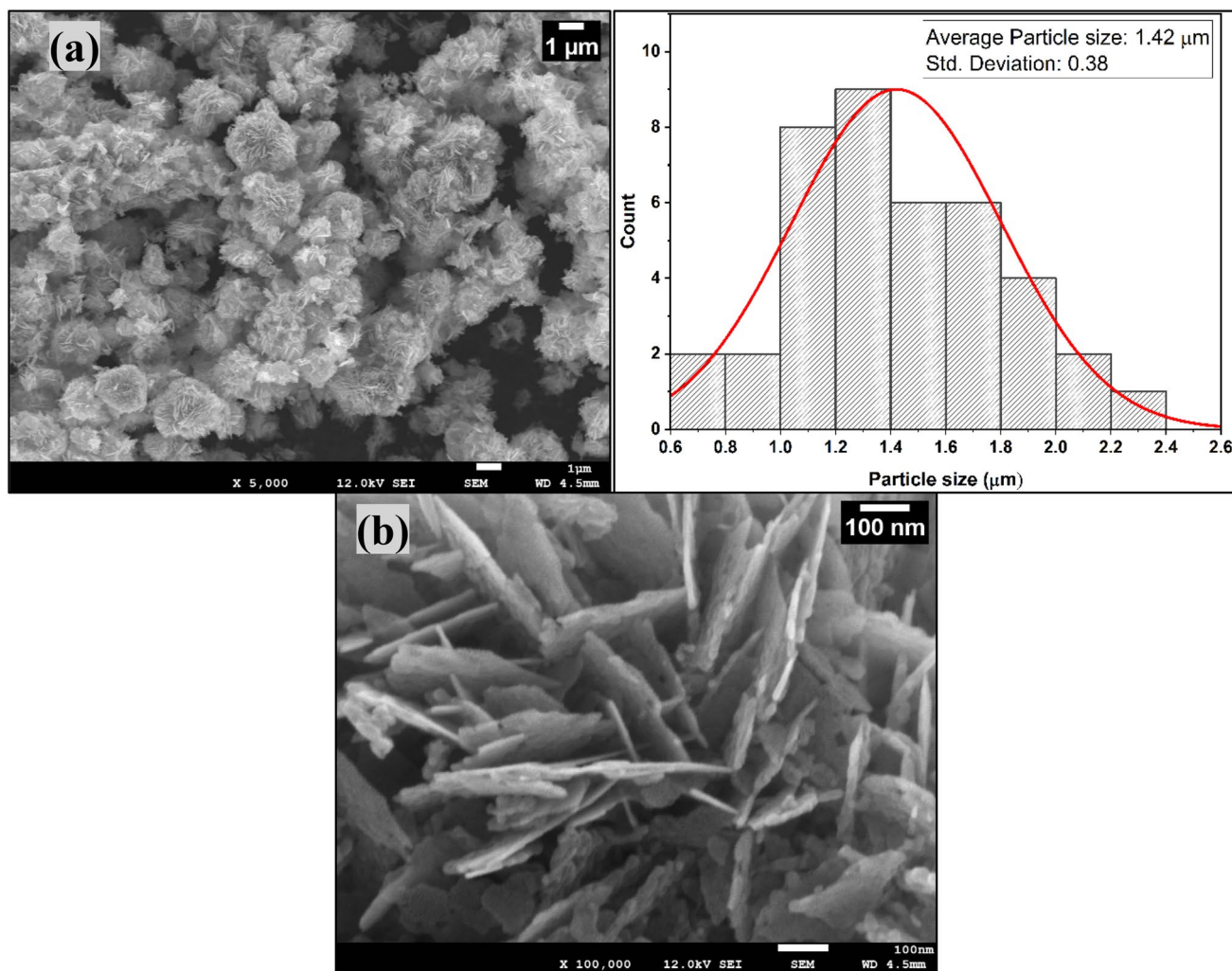The surface area of the samples was calculated using the Brunauer–Emmett–Teller (BET) technique, while

Fig. 5 a Flower-like structure of Zinc Oxide nanostructure along with the particle size distribution (FESEM), **b** Enlarged FESEM image of Pristine Zinc Oxide nanostructures

the pore size and the pore volume were analysed using the Barrett–Joyner–Halenda (BJH) method. Figure 9a demonstrates that the 1%, 2.5%, 5% and 7.5% Fe doped ZnO as well as the pristine ZnO all exhibit a typical type IV N_2 adsorption–desorption isotherm. Presence of the developed mesopores was indicated by the significant openings found in all the hysteresis loops. 2.5% and 5% Fe doped ZnO catalysts showed sharp increase in the adsorption amount in the P/P_0 range of 0.8–1.0 showing presence of well-developed mesopores indicating strong multiplayer adsorption.

Table 3 shows the surface area, pore volume and pore size of the samples. It is apparent that with integration of Fe ions in the ZnO crystals significantly enhanced the surface area. Again, 2.5 and 5% Fe doped ZnO catalysts showed the most specific surface area indicating high adsorption capacity (Fig. 9b). The same specimens exhibited high pore size indicating higher surface area per unit volume compared to the other samples (Table 3). This indicates the low surface energy of the 2.5 and 5% Fe doped samples predicting their higher photostability.

3.6 Photocatalytic studies

Assuming first order kinetics, degradation efficiency of the synthesized nanocatalysts can be obtained using Beer–Lambert's law, which states that the absorbance of radiation by a solute is directly proportional to its concentration.
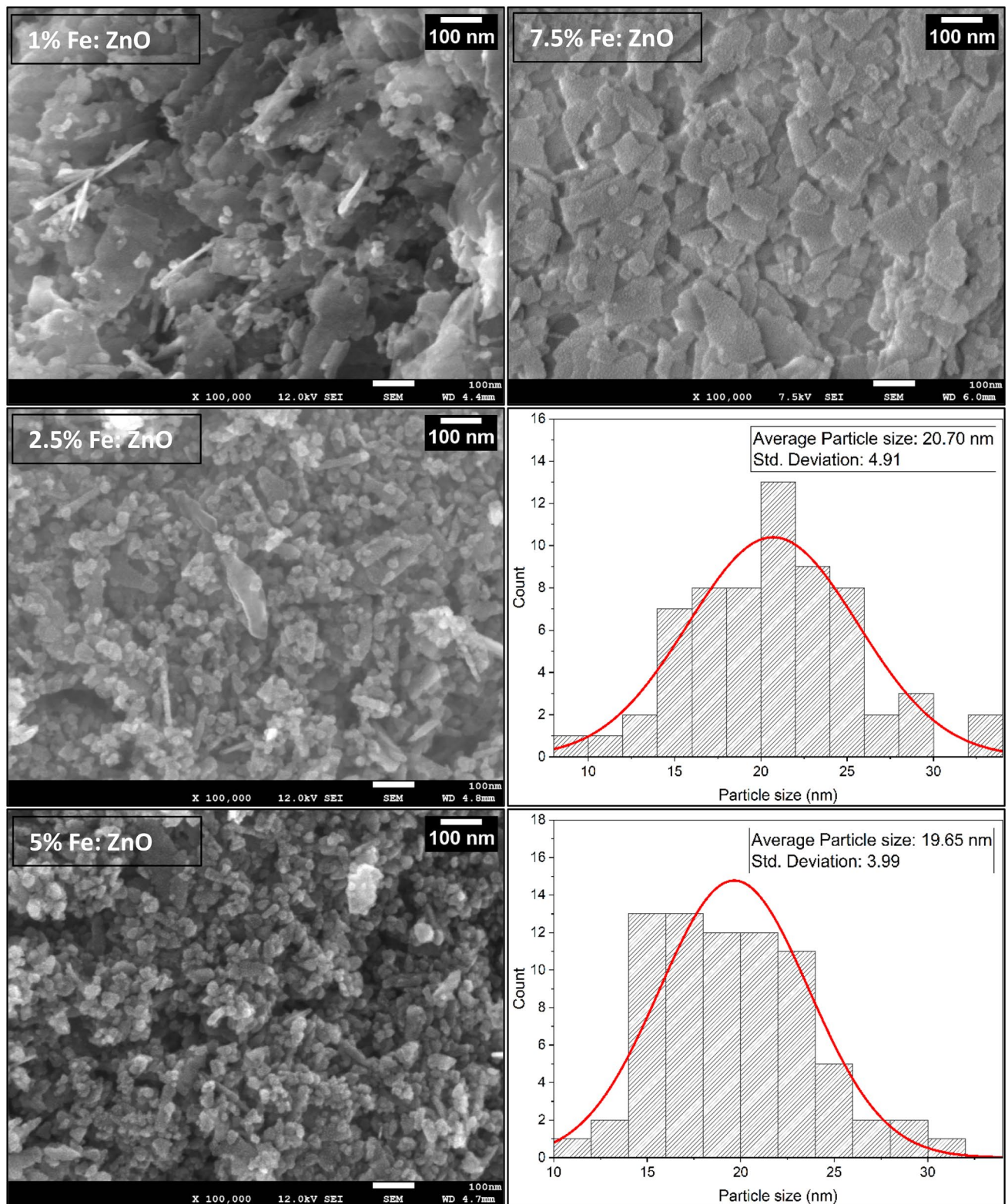
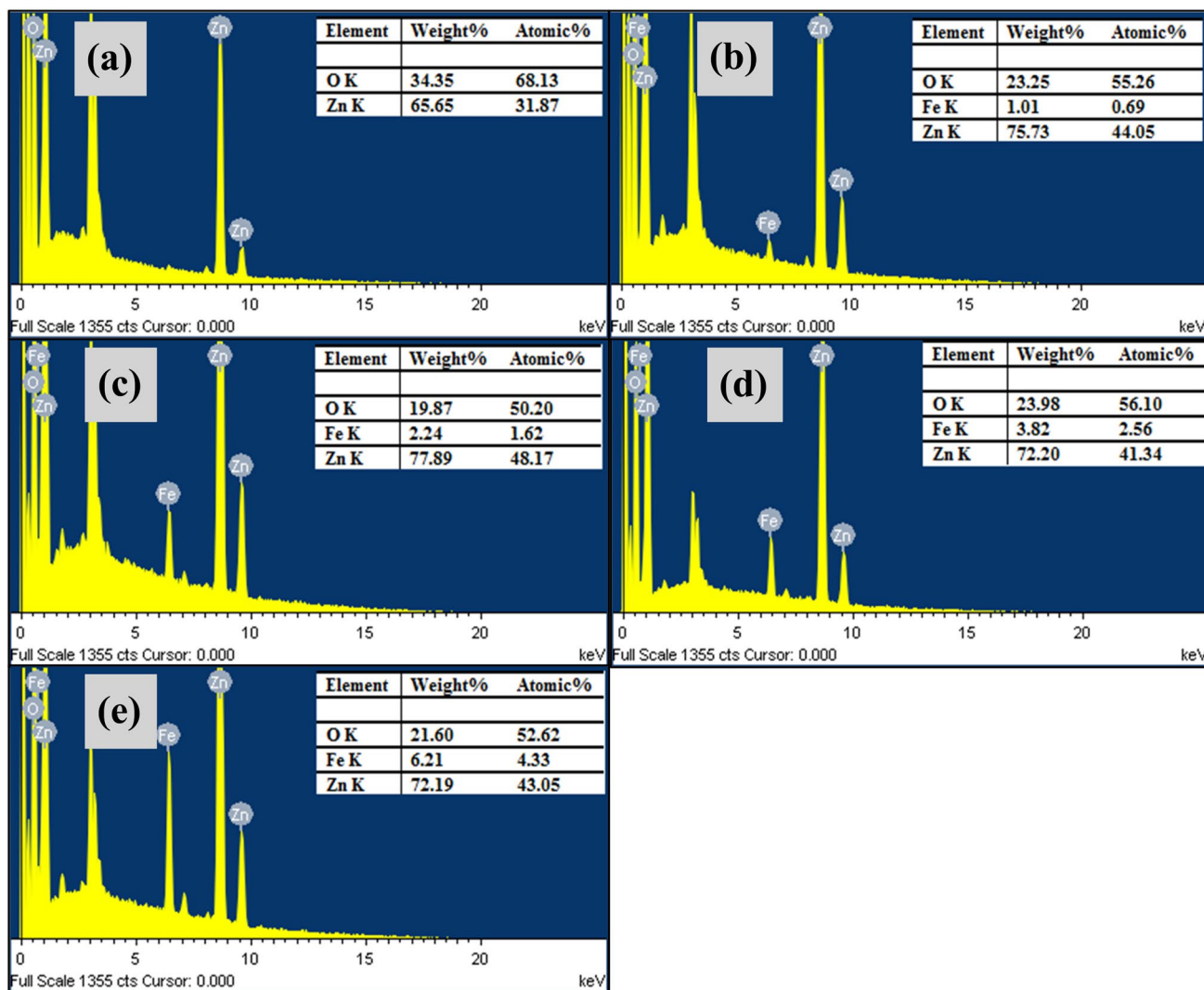**Fig. 6** FESEM images for Fe Doped ZnO nanostructures

Fig. 7 Elemental composition of **a** ZnO, **b** 1%, **c** 2.5%, **d** 5%, **e** 7.5% Fe Doped ZnO

Table 3 The optical band gap obtained from the Tauc Plots, BET specific surface area, pore volume and the pore size of the samples along with elemental composition obtained from EDS

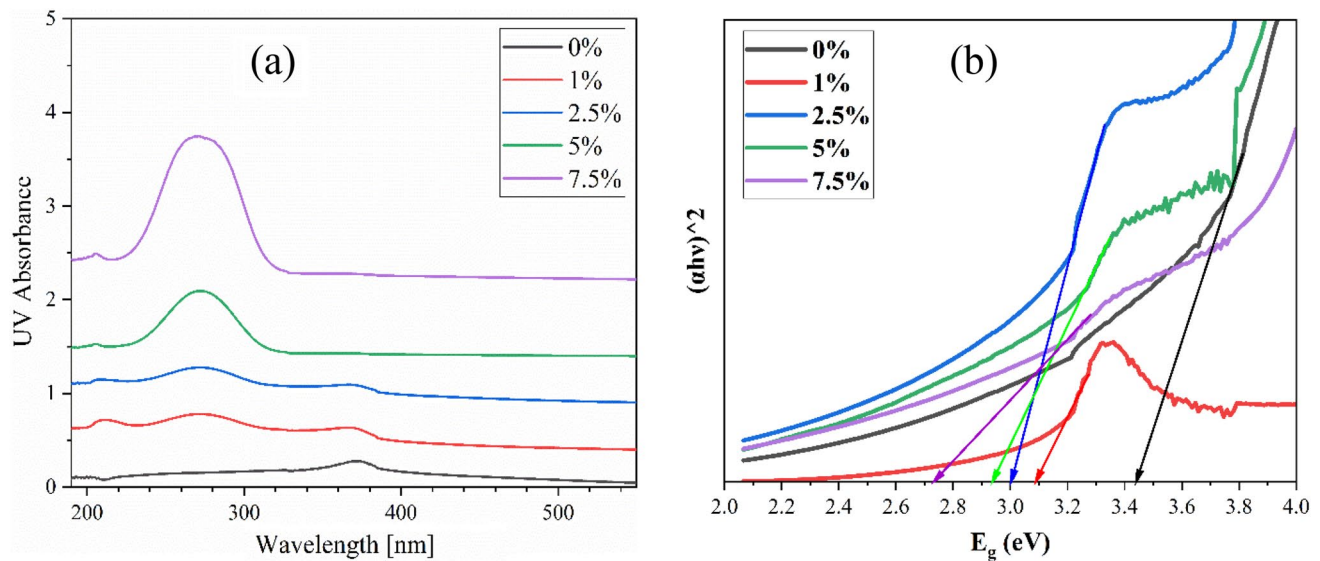| Photocatalyst	Band Gap (eV)	BET Surface Area (m^2/g)	Pore Volume (cm^3/g)	Pore Size (Å)	Elemental Composition (EDS)			
					Fe%	Zn%	O%	Fe/Zn
ZnO	3.44	22.198	0.07707	69.44	0	65.65	34.35	0
1% Fe:ZnO	3.09	33.472	0.07996	47.78	1.01	75.73	23.25	0.013337
2.5% Fe:ZnO	3.00	52.847	0.1869	70.75	2.24	77.89	19.87	0.028759
5% Fe:ZnO	2.94	53.599	0.1866	69.64	3.82	72.2	23.98	0.052909
7.5% Fe:ZnO	2.73	48.187	0.127	52.73	6.21	72.19	21.6	0.086023

Fig. 8 **a** UV–VIS absorbance spectra of Fe doped ZnO samples separated by an offset **b** Tauc plots for Fe: ZnO samples (0%, 1%, 2.5%, 5%, 7.5%)

$$\%D = \frac{C_0 - C_t}{C_0} * 100 = \frac{A_0 - A_t}{A_0} * 100 \quad (5)$$

where, D is the degradation percentage of the dye, C_0 is the concentration before irradiation, C_t is the concentration of the dye in the aqueous medium after t time, A_0 is the absorbance before irradiation and A_t is the absorbance after irradiation.

Pseudo first order rate kinetics for the dye degradation was considered, where rate constant was calculated using the following equation:

$$k = \frac{1}{t} \ln[\frac{C_0}{C_t}] \quad (6)$$

The degradation of Malachite Green and Crystal Violet can be seen in Fig. 10a–d. In presence of synthesized ZnO catalysts, the concentration of the dyes can be seen degrading significantly. After 20 min, 81.55% of the Malachite Green and 58.41% of the Crystal Violet were degraded. On doping of ZnO matrix with the Fe^{3+} ions, this rate of degradation also changed dramatically [Table 4]. Percentage degradation of the Malachite Green in 20 min improved to 93.88% on 1% doping, 97.29% on 2.5% doping, 99.05% on 5% doping, and 97.69% on 7.5% doping. Similar trend was found in case of Crystal Violet degradation verifying the superiority of 5% Fe doped ZnO catalyst over the others. It degraded 96.85% of Crystal Violet in 20 min.

These results can be correlated with the adsorption capacity and the pore volume of the synthesized catalysts. 5% Fe doped showed the highest capacity of adsorption in BET studies and also showed highest Specific Surface Area (SSA) among others. Morphological studies using FESEM also showed the isotropic nature of synthesized 5% Fe doped ZnO suggesting higher availability of adsorption sites. Table 5 compares the results of this study with the results from the recent studies on transition metal doped ZnO nanoparticles.

Also, the photocatalytic efficiency of 5% Fe doped ZnO NPs was tested in 3 cycles to investigate their recyclability and stability. The degradation percentages of MG in 20 min after each cycle are shown in Fig. 11, which shows the degradation % to be 99.05%, 98.36% and 97.12%. Moreover, the degradation percentages of CV in the same time interval were 96.85%, 93.05% and 89.6% after first three cycles. These results show good recyclability and stability of the 5% Fe doped ZnO NPs. The decrease in the degradation after recycling might be the reduction in surface active sites and some loss of catalysts during the recycling test [35].

3.7 Photocatalytic mechanism

The proposed mechanism of photocatalytic dye degradation using Fe^{3+} doped Zinc oxide nanoparticles is given in Fig. 12. Typically, when semiconductor
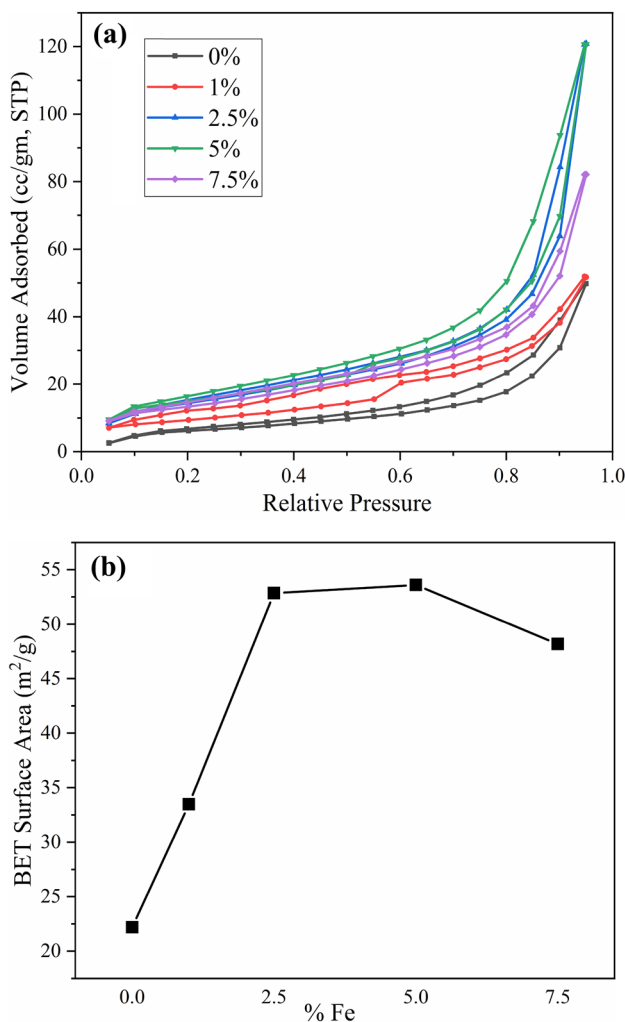
Fig. 9 a N$_2$ adsorption–desorption isotherms of the Fe doped ZnO nanocatalysts, **b** variation of specific surface area with dopant percentage

metal oxide photocatalysts are irradiated by light with energy higher than the band gap, electrons (e$^-$) from the valence band are excited to the conduction band leaving holes (h$^+$) in the valence band. The generated electron–hole pair takes part in redox reactions with O$_2$ from the atmosphere and H$_2$O from the solution to form active radicals ·O$_2^-$ and ·OH. These in turn react with the dyes/organic pollutants to convert them into harmless products such as H$_2$O, CO$_2$ [61–63] etc. This process is called as Photocatalysis or Photosensitization. Most of the electrons recombine with the respective holes after very short intervals. This recombination process though can be slowed down by metal doping [64, 65]. In Fe^{3+} doped ZnO NPs, Fe^{3+} ions act as electron reservoir and participate in charge

transfer with the ZnO NPs. This process slows down the recombination rate of electron hole pairs leading to increased photocatalytic activity of ZnO NPs.

3.8 Antibacterial studies

Antibacterial activity is evaluated by using the disk diffusion method against two bacterial strains. It is observed that pristine ZnO nanoflower as well as various concentrations Fe doped ZnO nanoflower show significant antibacterial activity against tested bacterial strains. Images of Petri plates showing inhibition zone after a 24 h incubation period are shown in Fig. 13a for *Staphylococcus Aureus* and b for *Escherichia coli*. Obtained result measurements are represented in Table 4 and demonstrate that pristine ZnO as well as Fe-doped ZnO show better antibacterial activity against *Staphylococcus Aureus (Gram positive bacteria)* as compared to *Escherichia Coli (Gram negative bacteria)* (Fig. 14), which is in agreement with previous reports [66]. This is due to the extra outer membrane on the cell walls of gram negative bacteria consisting of lipopolysaccharide and peptidoglycan, which helps them reduce the resistance by ZnO nanoparticles [67].

Also, Fe-doped ZnO nanostructure exhibited better antibacterial activity compared to pristine ZnO against both bacterial strains. It can be seen clearly that 5% Fe-doped ZnO (5ZF) displayed significantly improved antibacterial activity among all tested samples. The observed antibacterial activity is attributed to morphology with a higher surface area to volume ratio along with the optical properties of Fe-doped ZnO nanoparticles. Theoretically, ZnO produces reactive species (Zn^{2+} ions, superoxide radicals, hydroxyl radicals etc.) in solvents that actively oppose the growth of bacterial cells. These species interrupt the permeability of bacterial cell walls, hampering the protein synthesis and DNA replication process [68].

4 Conclusions

In this paper, Wurtzite Fe-doped ZnO nano catalysts were synthesized with varying dopant concentrations. With increasing dopant concentration up to 5%, crystalline size decreased, the adsorption capacity of the nanoparticles increased, optical band gap decreased. Also, significant changes in the morphology of the samples were observed after doping. Instead of the nanoflowered
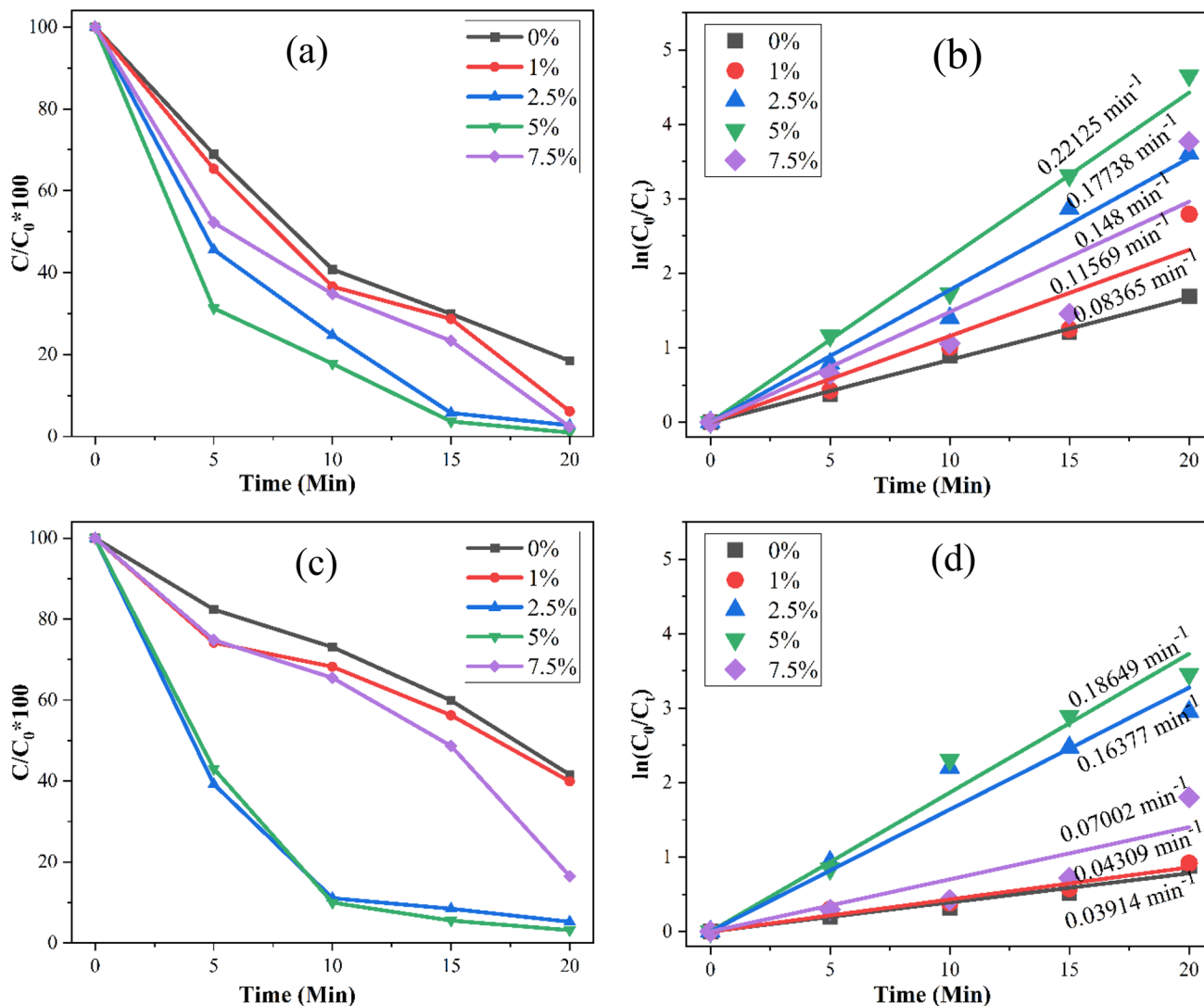
Fig. 10 Degradation of Malachite Green: **a** Dye percentage (C/C$_0$*100) vs. irradiation time and **b** Rate kinetics of degradation, Degradation of Crystal Violet: **c** Dye percentage (C/C$_0$*100) vs. irradiation time and **d** Rate kinetics of degradation (Color figure online)

Table 4 Rate constant and % degradation of the dyes after 120 min of irradiation, zone of inhibition obtained in antibacterial testing by a disk diffusion assay
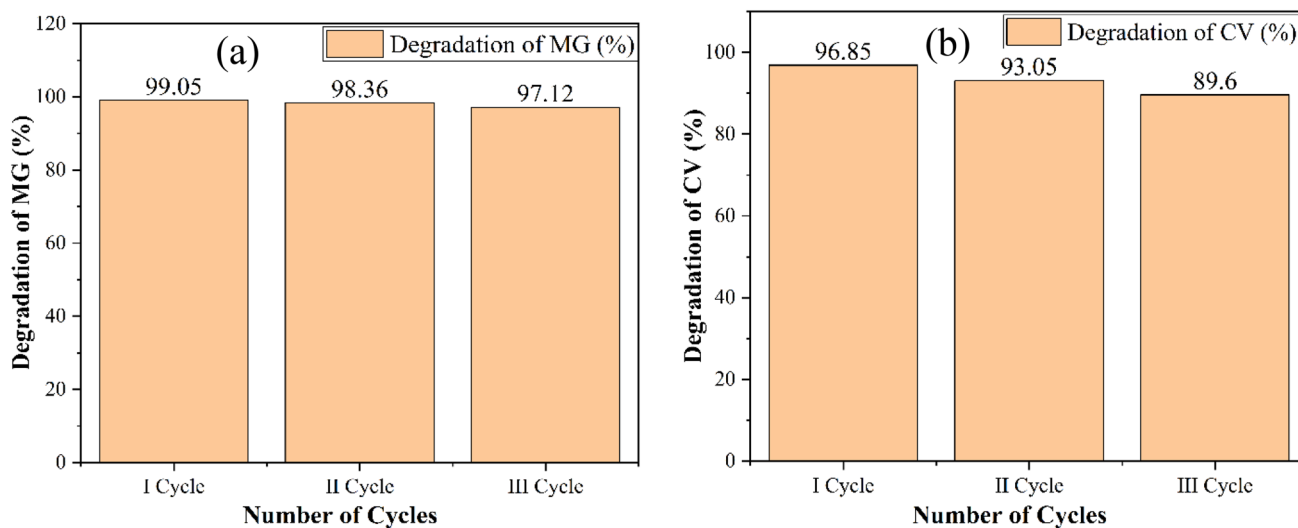
Dopant %	Malachite green				Crystal violet				Inhibition zone (mm)	
	k (min^{-1})	%	Half life (min)	R^2	k (min^{-1})	%	Half life (min)	R^2	*S. aureus*	*E. Coli*
0	0.08365	81.59	8.29	0.99	0.03914	58.42	17.71	0.98	9.92	7.01
1	0.11569	93.88	5.99	0.95	0.04309	60.09	16.09	0.99	9.89	8.21
2.5	0.17738	97.29	3.91	0.99	0.16377	94.78	4.23	0.98	10.02	7.48
5	0.22125	99.05	3.13	0.98	0.18649	96.85	3.72	0.99	10.56	10.06
7.5	0.148	97.69	4.68	0.92	0.07002	83.50	9.90	0.91	9.96	8.38

pristine ZnO nanoparticles, uniformly spherical nanoparticles with larger surface area and smaller size were obtained after 5% doping. These measured parameters correlate perfectly with the observed photocatalytic ability of the samples towards Malachite Green and Crystal Violet dyes. On 5% Fe

Table 5 Comparison of photocatalytic activities in current and reported studies of various studies of ZnO based catalysts

Catalyst	Synthesis method	Dye	Light source	Dye concentration (PPM)	Catalyst concentration (gm/L)	Time duration	Efficiency %	References
Ce/ZnO	Sonochemical	Crystal violet	Sunlight	50	0.2	100	99	[69]
Sn/ZnO	Coprecipitation	Methylene blue	Sunlight	20	1	180	95	[70]
Sn/ZnO	Precipitation	Methyl orange	Sunlight	10	0.3	120	99	[71]
Ag/ZnO	Hydrothermal	Methylene blue	Sunlight	10	0.5	210	92	[72]
Ir/ZnO with $K_2S_2O_8$	Chemical method	Malachite green	Sunlight	0.1	0.2	120	90	[73]
Ce/ZnO/Chitosan	Microwave synthesis	Malachite green	Sunlight	5	0.03	60	100	[74]
Ce/ZnO	Sol–gel	Methylene blue	Sunlight	80	5	120	92	[75]
Cu/ZnO	Wet chemical method	Methyl orange	Sunlight	10	0.3	120	99	[76]
Fe/ZnO	Co precipitation	Methyl orange	Sunlight	32	0.45	70	71	[77]
Fe/ZnO	Co precipitation	Malachite green	UV lamp (450W)	10	0.2	20	99.05	Present Work
		Crystal violet		10	0.2	20	96.85	

Fig. 11 Plot of % of degradation after 20 min of **a** Malachite Green **b** Crystal Violet (in presence of 5% Fe doped ZnO) versus the number of cycles (Color figure online)

doping, photocatalytic degradation of the dyes (after 120 min) improved from 73.35 to 98.07% in the case of Malachite Green and from 56.06 to 94.79% in the case of Crystal Violet. Antibacterial activity of the ZnO nanoparticles towards S. Aureus and E. Coli also improved significantly on Fe doping and 5% Fe doped ZnO proved to be the most effective antibacterial agent.

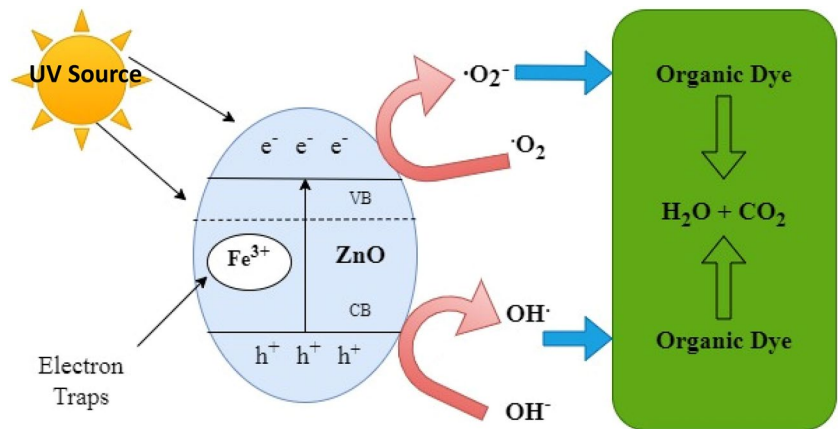**Fig. 12** Proposed photo-catalytic mechanism of Fe^{3+} doped ZnO NPs

Fig. 13 Disk diffusion assay using **a** *S. aureus*, **b** *E. coli* bacteria
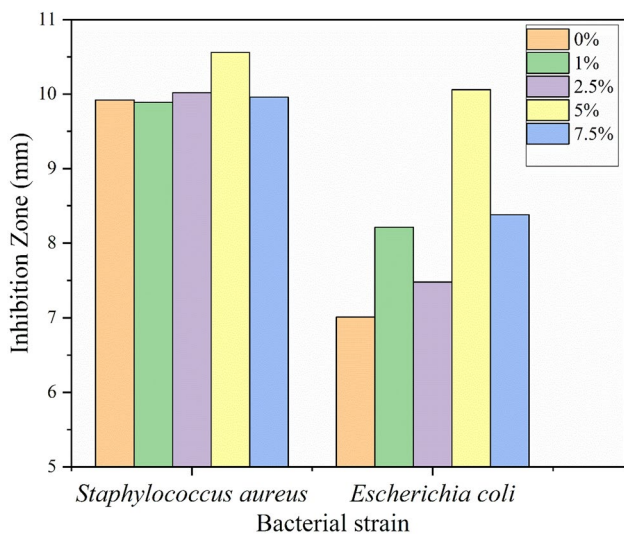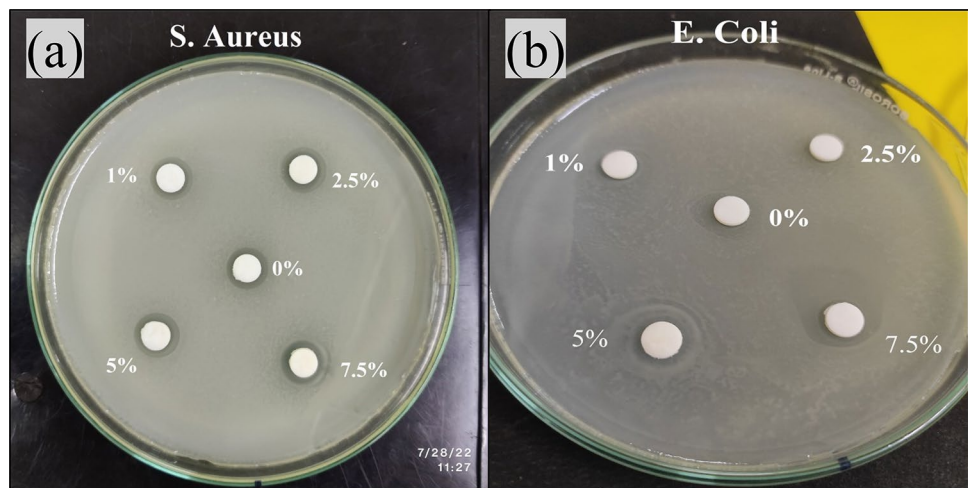

Fig. 14 Zone of inhibition for *S. aureus* and *E. coli* using Fe: ZnO nanoparticles

Acknowledgements

Author contributions

ARP: Conceptualization, Investigation, Formal Analysis, Writing—Original Draft. KRS: Data Curation, Formal Analysis. ADS: Validation, Methodology. PBU: Writing—Review & Editing, Supervision, Project Administration.

Funding

Data availability

We have provided all the data in the manuscript. However, additional data will be made available on reasonable request.

Declarations

Competing interests   The authors report no conflict of interest.

References

1. K. Tang, G. Wu, P. Zhang, C. Zhou, J. Liu, Sep. Purif. Technol. **115**, 83 (2013)
2. C. Santhosh, V. Velmurugan, G. Jacob, S.K. Jeong, A.N. Grace, A. Bhatnagar, Chem. Eng. J. **306**, 1116 (2016)
3. N.P. Raval, P.U. Shah, N.K. Shah, Appl. Water Sci. **7**, 3407 (2017)
4. S. Mani, R.N. Bharagava, Rev. Environ. Contam. Toxicol. **237**, 71 (2016)
5. S. Srivastava, R. Sinha, D. Roy, Aquat. Toxicol. **66**, 319 (2004)
6. A. Mittal, J. Mittal, A. Malviya, D. Kaur, V.K. Gupta, J. Colloid Interface Sci. **343**, 463 (2010)
7. G. Crini, E. Lichtfouse, Environ. Chem. Lett. **17**, 145 (2019)
8. Y. Ge, H. Luo, J. Huang, Z. Zhang, Opt. Mater. (Amst). **115**, 111058 (2021)
9. A.M. Huerta-Flores, E. Luévano-Hipólito, L.M. Torres-Martínez et al., J. Mater. Sci. Mater. Electron. **30**, 18506 (2019)
10. D. Chen, A. Wang, M.A. Buntine, G. Jia, ChemElectroChem **6**, 4709 (2019)
11. J.C. Cano-Franco, M. Álvarez-Láinez, Mater. Sci. Semicond. Process. **90**, 190 (2019)
12. A. Dey, Mater. Sci. Eng. B Solid-State Mater. Adv. Technol. **229**, 206 (2018)
13. X. Wang, Y. Yu, C. Yang, C. Shao, K. Shi, L. Shang, F. Ye, Y. Zhao, Adv. Funct. Mater. **31**, 1 (2021)
14. P.S. Basavarajappa, S.B. Patil, N. Ganganagappa, K.R. Reddy, A.V. Raghu, C.V. Reddy, Int. J. Hydrogen Energy **45**, 7764 (2020)
15. U. Alam, A. Khan, D. Ali, D. Bahnemann, M. Muneer, RSC Adv. **8**, 17582 (2018)
16. R.K. Mandal, P. Saha, T.P. Majumder, Optik (Stuttg). **246**, 167795 (2021)
17. V. Kumari, A. Mittal, J. Jindal, S. Yadav, N. Kumar, Front. Mater. Sci. **13**, 1 (2019)
18. M. Suresh, A. Sivasamy, J. Mol. Liq. **317**, 114112 (2020)
19. C.H. Nguyen, M.L. Tran, T.T. Van Tran, R.S. Juang, Sep. Purif. Technol. **232**, 115962 (2020)
20. R. Qin, F. Meng, M.W. Khan, B. Yu, H. Li, Z. Fan, J. Gong, Mater. Lett. **240**, 84 (2019)
21. P. Nayebi, M. Babamoradi, Optik (Stuttg). **244**, 167497 (2021)
22. M.T. Noman, N. Amor, M. Petru, A. Mahmood, P. Kejzlar, Polymers (Basel). **13**, 2227 (2021)
23. R. Manimozhi, M. Mathankumar, A.P.G. Prakash, Optik (Stuttg). **229**, 165548 (2021)
24. M. Ahmed, S. Mabrouk, R. Khaled, Opt. Mater. (Amst). **115**, 111039 (2021)
25. H. Helmiyati, N. Fitriana, M.L. Chaerani, F.W. Dini, Opt. Mater. **124**, 111982 (2022)
26. M. Rajasekaran, A. Arunachalam, P. Kumaresan, Mater. Res. Express **7**, 036412 (2020)
27. A.A. Menazea, N.S. Awwad, J. Mater. Res. Technol. **9**, 9434 (2020)
28. F. Naz, K. Saeed, Inorg. Nano-Metal Chem. **51**, 1 (2021)
29. L. Anju Chanu, W. Joychandra Singh, K. Jugeshwar Singh, K. Nomita Devi, Res. Phys. **12**, 1230 (2019)
30. S. Boulahlib, K. Dib, M. Ozacar, Y. Bessekhouad **113**, 110889 (2021)
31. P. Pascariu, I.V. Tudose, M. Suchea, E. Koudoumas, N. Fifere, A. Airinei, Appl. Surf. Sci. **448**, 481 (2018)
32. I.N. Reddy, C.V. Reddy, M. Sreedhar, J. Shim, M. Cho, D. Kim, Mater. Sci. Eng. B Solid-State Mater. Adv. Technol. **240**, 33 (2019)
33. L. Liu, Z. Liu, Y. Yang, M. Geng, Y. Zou, M.B. Shahzad, Y. Dai, Y. Qi, Ceram. Int. **44**, 19998 (2018)
34. J. Xie, H. Wang, M. Duan, L. Zhang, Appl. Surf. Sci. **257**, 6358 (2011)
35. Y. Mao, Y. Li, Y. Zou, X. Shen, L. Zhu, G. Liao, Ceram. Int. **45**, 1724 (2019)
36. T. Ozkaya, M.S. Toprak, A. Baykal, H. Kavas, Y. Köseoğlu, B. Aktaş, J. Alloys Compd. **472**, 18 (2009)
37. K. Kusdianto, T.D. Sari, M.A. Laksono, S. Madhania, S. Winardi, I.O.P. Conf, Ser. Mater. Sci. Eng. **1053**, 012023 (2021)

38. A.T. Ravichandran, R. Karthick, Res. Mater. **5**, 100072 (2020)

39. S. Singhal, J. Kaur, T. Namgyal, R. Sharma, Phys. B Condens. Matter **407**, 1223 (2012)

40. M. Mittal, M. Sharma, O.P. Pandey, Sol. Energy **110**, 386 (2014)

41. S. Roguai, A. Djelloul, Solid State Commun. **334**, 114362 (2021)

42. A. Ashrafi, C. Jagadish, J. Appl. Phys. **102**, 071101 (2007)

43. V. Moleyar, P. Narasimham, Int. J. Food Microbiol. **16**, 337 (1992)

44. D. Varshney, K. Verma, S. Dwivedi, Optik (Stuttg). **126**, 4232 (2015)

45. U. Holzwarth, N. Gibson, Nat. Publ. Gr. **6**, 534 (2011)

46. N. Siva, D. Sakthi, S. Ragupathy, V. Arun, N. Kannadasan, Mater. Sci. Eng. B Solid-State Mater. Adv. Technol. **253**, 114497 (2020)

47. A. Khorsand Zak, W.H. Abd Majid, M.E. Abrishami, R. Yousefi, Solid State Sci. **13**, 251 (2011)

48. A.K. Srivastava, M. Deepa, N. Bahadur, M.S. Goyat, Mater. Chem. Phys. **114**, 194 (2009)

49. J. Anghel, A. Thurber, D.A. Tenne, C.B. Hanna, A. Punnoose, J. Appl. Phys. **107**, 1019 (2010)

50. M. Naeem, S.K. Hasanain, A. Mumtaz, J. Phys. Condens. Matter. **20**, 025210 (2008)

51. M.M. Ba-Abbad, A.A.H. Kadhum, A.B. Mohamad, M.S. Takriff, K. Sopian, Chemosphere **91**, 1604 (2013)

52. M. Mehedi Hassan, A.S. Ahmed, M. Chaman, W. Khan, A.H. Naqvi, A. Azam, Mater. Res. Bull. **47**, 3952 (2012)

53. K.A. Salazar, V.C. Agulto, M.J.F. Empizo, K. Shinohara, K. Yamanoi, T. Shimizu, N. Sarukura, A.C.C. Yago, P. Kidkhunthod, S. Sattayaporn, V.A.I. Samson, R.V. Sarmago, J. Cryst. Growth **574**, 126332 (2021)

54. B. Babu, G. Thirumala Rao, V. Pushpa Manjari, K. Ravindranadh, R. Joyce Stella, R.V.S.S.N. Ravikumar, J. Mater. Sci. Mater. Electron. **25**, 4179 (2014)

55. K.N. Devi, S.A. Devi, W.J. Singh, K.J. Singh, J. Mater. Sci. Mater. Electron. **32**, 8733 (2021)

56. S. Sankadiya, N. Oswal, P. Jain, N. Gupta, PAIP Conf. Proc. **1724**, 3 (2016)

57. R. Zamiri, A.F. Lemos, A. Reblo, H.A. Ahangar, J.M.F. Ferreira, Ceram. Int. **40**, 523 (2014)

58. A. Sahai, Y. Kumar, V. Agarwal, S.F. Olive-Méndez, N. Goswami, J. Appl. Phys. **116**, 164315 (2014)

59. M. Cernea, V. Mihalache, E.C. Secu, R. Trusca, V. Bercu, L. Diamandescu, Superlattices Microstruct. **104**, 362 (2017)

60. S.J. Priscilla, R. Daniel, Y. Dhakshayani, S.C. Caroline, K. Sivaji, Mater. Today Proc. **36**, 793 (2019)

61. S.I. Shanthi, S. Poovaragan, M.V. Arularasu, S. Nithya, R. Sundaram, C.M. Magdalane, K. Kaviyarasu, M. Maaza, J. Nanosci. Nanotechnol. **18**, 5441 (2018)

62. K.V. Karthik, A.V. Raghu, K.R. Reddy, R. Ravishankar, M. Sangeeta, N.P. Shetti, C.V. Reddy, Chemosphere **287**, 132081 (2022)

63. L.T.T. Nguyen, L.T.H. Nguyen, A.T.T. Duong, B.D. Nguyen, N.Q. Hai, V.H. Chu, T.D. Nguyen, L.G. Bach, Materials (Basel) **12**, 1 (2019)

64. R. Ebrahimi, K. Hossienzadeh, A. Maleki, R. Ghanbari, R. Rezaee, M. Safari, J. Environ. Health Sci. Eng. **17**, 79 (2019)

65. M. Faraz, F.K. Naqvi, M. Shakir, N. Khare, New J. Chem. **42**, 2295 (2018)

66. K.R. Ahammed, M. Ashaduzzaman, S.C. Paul, M.R. Nath, S. Bhowmik, O. Saha, M.M. Rahaman, S. Bhowmik, T. Das Aka, SN Appl. Sci. **2**, 1 (2020)

67. A.D. Russell, J. Antimicrob. Chemother. **52**, 750 (2003)

68. K. Kannan, D. Radhika, S. Vijayalakshmi, K.K. Sadasivuni, A.A. Ojiaku, U. Verma, Int. J. Environ. Anal. Chem. **00**, 1 (2020)

69. S.P. Meshram, P.V. Adhyapak, S.K. Pardeshi, I.S. Mulla, D.P. Amalnerkar, Powder Technol. **318**, 120 (2017)

70. N. Venkatesh, S. Aravindan, K. Ramki, G. Murugadoss, R. Thangamuthu, P. Sakthivel, Environ. Sci. Pollut. Res. **28**, 16792 (2021)

71. J.Z. Li, J.B. Zhong, W. Hu, Y. Lu, J. Zeng, Y.C. Shen, Mater. Sci. Semicond. Process. **16**, 143 (2013)

72. D. Kwon, J. Kim, Korean J. Chem. Eng. **37**, 1226 (2020)

73. N. Babajani, S. Jamshidi, J. Alloys Compd. **782**, 533 (2019)

74. A.M. Saad, M.R. Abukhadra, S. Abdel-Kader Ahmed, A.M. Elzanaty, A.H. Mady, M.A. Betiha, J.J. Shim, A.M. Rabie, J. Environ. Manag. **258**, 110043 (2020)

75. S. Karidas, B.K. Veena, N. Pujari, P. Krishna, V. Chunduru, Sadhana Acad. Proc. Eng. Sci. **45**, 1 (2020)

76. P.M. Perillo, M.N. Atia, Mater. Today Commun. **17**, 252 (2018)

77. K. Kumar, M. Chitkara, I.S. Sandhu, D. Mehta, S. Kumar, J. Alloys Compd. **588**, 681 (2014)